Investigating wind-driven Snow Redistribution Processes over an Alpine Glacier with high-resolution Terrestrial Laser Scans and Large-eddy Simulations

Annelies Voordendag[1,*], Brigitta Goger[1,2,*], Rainer Prinz[1], Tobias Sauter[3], Thomas Mölg[4], Manuel Saigger[4], and Georg Kaser[1]

[*]These authors contributed equally to this work.
[1]Department of Atmospheric and Cryospheric Sciences, Universität Innsbruck, Innsbruck, Austria
[2]Center for Climate Systems Modeling, ETH Zurich, Zurich, Switzerland
[3]Geographisches Institut, Humboldt-Universität zu Berlin, Berlin, Germany
[4]Climate System Research Group, Institute of Geography, Friedrich-Alexander-Universität Erlangen-Nürnberg, Erlangen, Germany

Correspondence: Annelies Voordendag (annelies.voordendag@uibk.ac.at), Brigitta Goger (brigitta.goger@c2sm.ethz.ch)

Abstract.

Wind-driven snow redistribution affects the glacier mass balance by eroding or depositing mass from or to different parts of the glacier's surface. High-resolution observations are used to test the ability of large eddy simulations as a tool for distributed mass balance modeling. We present a case study of observed and simulated snow redistribution over Hintereisferner glacier (Ötztal Alps, Austria) between 6 and 9 February 2021. Observations consist of three high-resolution Digital Elevation Models ($\Delta x=1$ m) derived from terrestrial laser scans taken shortly before, directly after, and 15 hours after snowfall. The scans are complemented by data sets from three onsite weather stations. After the snow fall event the snowpack decreased by 0.08 m on average over the glacier and typical snow redistribution patterns were observed. The decrease of the snow depth is to be attributed to both post-snowfall compaction and redistribution of snow. Simulations were performed with the WRF model at $\Delta x=48$ m with a newly implemented snow drift module. The spatial patterns of the simulated snow redistribution agree well with the observed generalized patterns. Snow redistribution contributed -0.026 m to the surface elevation decrease over the glacier surface on 8 Feb, resulting in a mass loss of -3.9 kg m^{-2}, which is in the same order of magnitude as the observations. With the single case study we cannot yet extrapolate to the impact of post-snowfall events on the seasonal glacier mass balance, but the study shows that the snow drift module in WRF is a powerful tool to improve knowledge on snow redistribution over glaciers and that the model setup can be applied to other mountain glaciers.

1 Introduction

The European mountain cryosphere is an important contributor to Alpine water availability and experiences - as the worldwide cryosphere - the effects of global climate warming (e.g. Fox-Kemper et al., 2021; Hock et al., 2022). The annual mass balances of the Alps' glaciers are increasingly more negative since the 1980's (Marzeion et al., 2012; Huss and Hock, 2018; Hugonnet

20 et al., 2021), and extreme glacier mass losses are observed in more recent years (Copernicus Climate Change Service (C3S), 2023; Voordendag et al., 2023b; Cremona et al., 2023). However, the impact of small-scale processes such as cryosphere-atmosphere exchange or wind-driven snow transport on snow accumulation over mountain glaciers still represent a knowledge gap (e.g. Mott et al., 2018; Beniston et al., 2018). Spatial observations of snow cover changes on mountain glaciers are sparse and often only available on the point scale, and numerical weather prediction models on the kilometre range are not able to

25 resolve the relevant small-scale boundary layer processes (e.g., surface fluxes) over highly mountainous terrain (Vionnet et al., 2016; Goger et al., 2018, 2019). On the other hand, distributed mass balance models (Machguth et al., 2006), e.g. COSIPY (Sauter et al., 2020), require high-resolution input fields to deliver respective information about a glacier's surface mass balance. Among the usual meteorological variables (e.g., temperature, wind speed, relative humidity, total precipitation, etc), snow depth can also be used as an initial condition, improving the accuracy of distributed surface mass balance models.

30

In general, snow depth distribution over complex terrain cannot be assumed to be homogeneous. The spatial precipitation pattern over mountains is heterogeneous due to multi-scale interactions of the atmospheric flow with topography (Frei and Schär, 1998; Isotta et al., 2013; Colle et al., 2013). Furthermore, during or after snowfall, the snowpack is affected by four processes: melt, compaction, sublimation, and wind-driven redistribution. Compaction of the snowpack can be driven by the

35 overburden of its own weight, the pressure exerted by the wind and/or snow metamorphosis processes including melting and refreezing. Snow redistribution is the relocation of wind-borne snow, or also called snow drift, from one part of the snow-covered area to another (Cogley et al., 2011; Mott et al., 2018). Redistributed snow leads to snow depth decrease in areas where snow is eroded, and snow cover increases, where snow particles are deposited. The resulting snow patterns strongly depend on the local topography, and the wind speed and direction (Gerber et al., 2017; Vionnet et al., 2013, 2021; Sauter et al.,

40 2013). The complex terrain makes mountain glaciers subject to heterogeneous snow cover distribution caused by both complex precipitation patterns and wind driven redistribution during and after snow fall (Dadic et al., 2010).

It is still a challenge to measure the spatial (re)distribution of the snow cover continuously in a complex alpine environment. One possible method to record glacier-wide snow distribution of precipitation and the post-snowfall surface elevation changes over a glacier is with repeated Digital Elevation Models (DEM) derived from terrestrial or airborne laser scanning (TLS/ALS).

45 In recent times, surface elevation changes at mountain glaciers were measured with both TLS (Fischer et al., 2016; Prantl et al., 2017; Xu et al., 2019; Mendoza et al., 2020) and ALS (Grünewald et al., 2014, , Table 2). However, these DEMs are acquired irregularly and at low temporal resolution. Data series that capture snow fall and snow redistribution thereafter are not available so far. This gap was addressed with the installation of a permanent TLS station nearby Hintereisferner glacier (HEF, Ötztal Alps, Austria) (Voordendag et al., 2021b). This TLS station acquires a daily DEM automatically, but even hourly acquisitions

50 are possible if manually initiated. A comprehensive uncertainty assessment shows that this TLS station is able to capture small changes at the glacier surface, such as snow (re)distribution (Voordendag et al., 2023a). The high temporal and spatial data resolution contribute to improving the process-understanding at HEF and can be used to validate surface elevation changes in atmospheric model simulations.

On the modelling side, high-resolution large-eddy simulations (LES, $\Delta x < 100\,\mathrm{m}$) over complex terrain have become a new possibility for process studies in recent years, e.g. foehn-cold air pool interactions (Umek et al., 2021) or snow accumulation patterns over complex alpine terrain (Gerber et al., 2018). Sauter and Galos (2016) explored with semi-idealized simulations the sensible heat flux pattern over an alpine glacier and found that its heterogeneity depends on the wind speed and direction. These results were confirmed by real-case LES by Goger et al. (2022) over HEF, finding that the turbulent surface fluxes on the glacier were strongly governed by the mesoscale flow direction and upstream conditions. However, all of the aforementioned studies focused on processes in the atmospheric boundary layer, but not on wintertime atmosphere-cryosphere exchange like wind-driven snow redistribution.

While most atmospheric numerical weather prediction (NWP) models include a multi-layer snow scheme in their land-surface models, e.g. the three layer NOAH-MP scheme in the Weather Research and Forecasting (WRF) model (Niu et al., 2011) or the multi-layer snow model in the Integrated Forecasting System (IFS, Arduini et al., 2019), the explicit treatment of wind-driven snow redistribution is often not implemented. Some studies couple full stand-alone snowpack models with NWP models. For example, Vionnet et al. (2014) coupled the Crocus snow model with the Meso-NH LES model to explore snow accumulation patterns. They found that the wind-induced snow redistribution is responsible for an increase in spatial variability in snow depth. The most recent development in this direction is CRYOWRF (Sharma et al., 2023), where SNOWPACK (Lehning et al., 1999) was coupled to the WRF model, also including a snow drift module. First results suggest that CRYOWRF can successfully simulate snow accumulation and redistribution both over the Antarctic and the Swiss Alps, but the disadvantage of this and other approaches is the extra coupling of the models with a (previously) stand-alone snowpack model.

In this work, we show a case study with high-resolution TLS observations of wind-driven snow redistribution on HEF. The worldwide unique setup of a permanent TLS station overlooking the glacier provides us with sub-daily observations at a horizontal resolution of 1 m. However, since the mere detection of change in snow depth does not allow for resolving the different processes at work, we estimate the different contributions to the snow depth change from discussing the weather conditions during the studied event as mirrored by on-site weather station data. In turn, we can evaluate simulations with the WRF model at $\Delta x = 48\,\mathrm{m}$ with a newly implemented snow drift module by Schmid (2021) with this rich observational data set. The simulations have the potential to resolve the main driving processes to snow surface depth change such as compaction and wind-driven snow redistribution. Finally, we assess the potential impact of these post-depositional processes of the snow cover on the glacier's mass balance.

2 Methods

This paper presents a case study between 6 and 9 February 2021. First, this section introduces the study area with its available observations and the case study selection. Second, we elaborate on the available TLS data. Last, the model setup and the novel snow drift module for this particular case study are introduced.

2.1 Study area and available observations

The Hintereisferner (HEF) is part of the Rofental catchment (Strasser et al., 2018) and is a principal research site to study glaciological processes and glacier mass balances since the early days of glacier research (Blümcke and Hess, 1899). Annual and seasonal glaciological mass balance measurements are acquired since 1952/53, and HEF is classified as one of the 'ref-
90   erence glaciers' by the World Glacier Monitoring Service (WGMS, Zemp et al., 2009). HEF has presently (2018) a length of approximately 6.3 km and stretches from its highest point, the Weißkugel (3738 m a.s.l.), down to a terminus altitude of 2460 m a.s.l.

The glacier and its surroundings are well-equipped with several automated weather stations (AWS). The major station for this study is *Im Hinteren Eis* (IHE), which is located on the orographic right side of the glacier on the ridge at the Austrian-Italian
95   border (Fig. 1). This measurement location is equipped with a permanently installed TLS, which is extensively described in Voordendag et al. (2021b, 2023a) and Section 2.3 of this study. Additionally, two webcams, which deliver images every thirty minutes[1], are installed at the position of the TLS and overlook the glacier surface. About 50 m from the container with the TLS, an eddy-covariance flux tower is installed at the mountain ridge (Table 1) providing, among the usual meteorological variables, observations of turbulence kinetic energy and surface fluxes. After post-processing (Stiperski and Rotach, 2016;
100 Rotach et al., 2017), the averaged variables are available in a 15-minute interval. The second location is *Station Hintereis* (StHE, Fig. 1a), located on the orographic left side of the glacier equipped with an AWS (Table 1) and a mountain hut used for logistical support. Last, a temporary AWS was installed at the glacier in the line of sight between IHE and StHE from 7 Dec, 2020 to 22 Feb, 2021. This station is called *AWS28* hereafter, as it was installed at an altitude of approximately 2800 m a.s.l.. It provides common meteorological measurements (Table 1). The meteorological observations from HEF are used to explain the
105 meteorological situation and to validate the simulations (see Sect. 2.4) on a point scale.

2.2 Case Study Selection

The case study has been selected based on the meteorological observations and the images recorded by the webcams by applying the following criteria:

- the period should be in winter and show a pronounced change of the synoptic weather situation with a subsequent
110   significant accumulation of fresh snow;

- wind speeds above $5\,\mathrm{m\,s^{-1}}$ should be observed during or directly after the snowfall event to ensure snowdrift;

- no surface elevation change due to melt should be observed;

- frequent TLS scans must be available (Sect. 2.3).

The time window of 6 Feb-9 Feb, 2021 met these criteria.

---

[1]www.foto-webcam.eu/webcam/hintereisferner1/
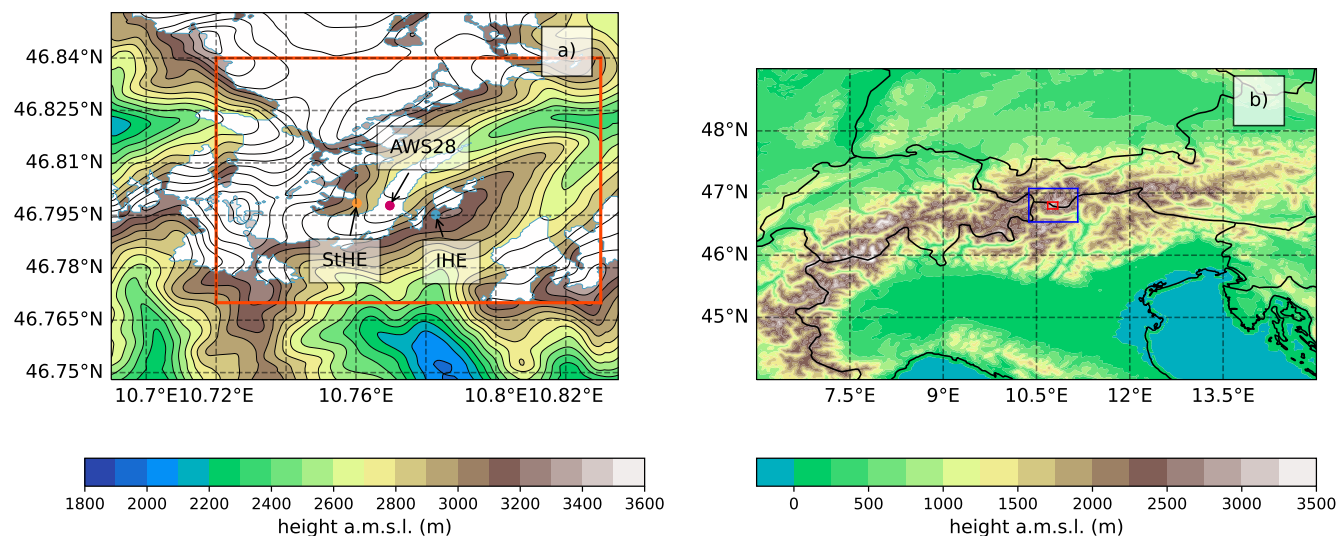
Figure 1. Panel a): Overview of the innermost model domain ($\Delta x = 48\,\mathrm{m}$, red rectangle) with the model topography (contour lines) and the glacier areas as represented in the model (white area with light blue outlines). The locations of the three stations StHE, AWS28, and IHE are highlighted in colors. Panel b): The mesoscale domain ($\Delta x = 1\,\mathrm{km}$) spanning the Alps with the two LES domains highlighted in blue ($\Delta x = 240\,\mathrm{m}$) and red ($\Delta x = 48\,\mathrm{m}$).

115   The large-scale synoptic situation from ERA5 reanalysis data revealed that on 6 Feb, a through was moving westward from France towards the Alps. The associated frontal system passed our area of interest in the early hours of 8 Feb. The frontal system was associated with pre-frontal snow fall, which ceased in the early morning hours of 8 Feb. After the through passage, winds at upper levels shift towards Westerlies, while at crest levels, winds shift to Westerlies to South-westerlies. At around 12 UTC, the wind speeds increased to over $5\,\mathrm{m\,s^{-1}}$, providing excellent snow drift conditions. Webcam imagery (Fig. 2) of 120   8 Feb, 15:30 local time (UTC+1) shows blowing snow at the mountain ridges surrounding the glacier, indicating high wind speeds and snow drift.

2.3   Terrestrial laser scanning acquisitions

The location IHE is equipped with a permanently installed and automated TLS station (Voordendag et al., 2021b). The TLS station is in operational daily use since 2020, and thus delivers a daily point cloud of HEF under clear weather conditions (e.g. 125   no clouds between TLS and target surface). The TLS station is normally set to a daily acquisition at 01:42 UTC, but as the end of a snowfall period was observed on the webcam images on 8 Feb, 10:22 UTC, an additional scan acquisition was initialized. This led to three usable scans for the case study: shortly before the snowfall event on 6 Feb (01:42 UTC), directly after the snowfall 8 Feb (10:22 UTC) and approximately 15 hours after snowfall ended on 9 Feb (01:42 UTC). In the following text, we refer to these scans as scan 1, 2, and 3, respectively. The acquired point clouds are registered to each other with the RiSCAN PRO 130   software (RIEGL, 2019) and gridded to Digital Elevation Models (DEMs) with an one-meter horizontal resolution. Voordendag

	Im Hinteren Eis	Station Hintereis	AWS28
Latitude	46.795761	46.798896	46.79779
Longitude	10.783409	10.760373	10.76967
Altitude (m a.s.l.)	3264	3031	2782
Air pressure	Setra278 CS100	Setra278 CS100	Vaisala PTB 110
Air temperature	Rotronic HC2-S3 Ventilated; at 1.50 m and 5.50 m	Campbell Scientific EE181 Naturally ventilated; at 2.10 m	Campbell Scientific CS215
Precipitation	Geonor T200B	Ott Pluvio2L	
Radiation	Kipp&Zonen CNR4	Kipp&Zonen CNR4	Kipp&Zonen CNR4
Relative humidity	Rotronic HC2-S3 Ventilated; at 1.50 m and 5.50 m	Campbell Scientific EE181 Naturally ventilated; at 2.10 m	Campbell Scientific CS215
Snow depth	Campbell Scientific SR50ATH-L	Campbell Scientific SR50A	Campbell Scientific SR50A
Wind speed and direction	Lufft Ventus-UMB At 1.50 m, 3.00 m and 6.00 m	Young 05103-45 Alpine At 3.30 m	Young 05103
3D sonic anemometer	Metek uSonic-3: At 3.18 m		
TLS	RIEGL VZ-6000		
Webcams	Canon EOS1200D (2x)		

Table 1. Location, altitude and available observations at Im Hinteren Eis, Station Hintereis and AWS28 during the period of the case study.
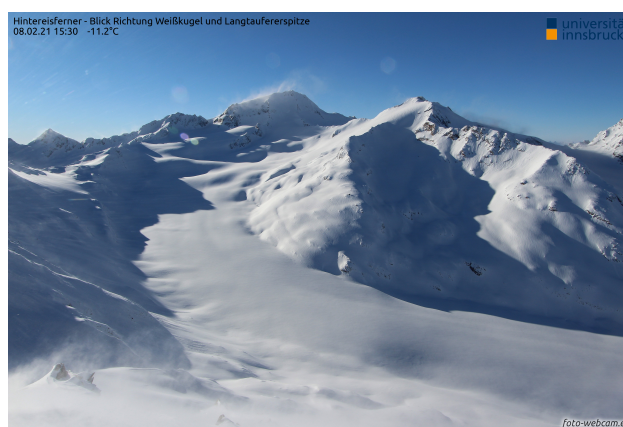
Figure 2. Webcam image of 8 Feb, 2021, 15:30 (UTC+1) showing signs of snow drift at the mountain ridges. The image is retrieved from https://www.foto-webcam.eu/webcam/hintereisferner1/2021/02/08/1530.

et al. (2023a) investigated surface change processes that can be captured by the TLS station: They found that the scans have an uncertainty of $\pm 0.10\,\mathrm{m}$ in vertical direction after the registration in RiSCAN PRO. Additionally, the high-resolution point clouds are gridded to DEMs with a $\Delta x = 48\,\mathrm{m}$ allowing a direct evaluation of the numerical simulations.

2.4 Numerical model

135 We employ the Weather Research and Forecasting (WRF) model version 4.1 (Skamarock et al., 2019) in a nested set-up for the numerical simulations of the case study period. The numerical setup is the same as described and used in Goger et al. (2022), therefore we only mention the most relevant aspects. As model boundary conditions, we use ERA5 reanalysis data, feeding the outermost WRF domain ($\Delta x = 6$ km) spanning Europe, and subsequently nesting down across $\Delta x = 1$ km (mesoscale domain) to the two LES domains at $\Delta x = 240$ m and $\Delta x = 48$ m, respectively. We put a special focus on the correct representation of

140 land-use and glacier outlines in the LES domains, therefore we use the CORINE land-use data set (European Environmental Agency, 2017) with an additional correction of the ice surfaces of the glaciers as described in Goger et al. (2022). NOAH-MP (Niu et al., 2011) is used as a land-surface scheme, which includes a three-layer snow model. Furthermore, we implemented a novel snow drift module as described in Section 2.4.1. We use the Thompson microphysics (Thompson et al., 2008), the MM5 revised surface layer scheme (Jiménez et al., 2012), and the RRTMG two-stream radiation scheme (Iacono et al., 2008) with

145 topographic shading for all domains. For the boundary layer turbulence we employ the MYNN parameterization (Nakanishi and Niino, 2009) for the two outermost domains, while we switch it off in the LES domains and employ the turbulence closure after Deardorff (1980). Furthermore, we also use the online averaging module by Umek et al. (2021), therefore, all model output shown in the following are 15-minute averages. The model is initialized on 8 Feb, 00 UTC, and runs for 24 hours. We would like to stress that the snowpack in the model is initialized at the same time. This might introduce a slight bias in

150 snowpack density, since the model initializes the snowpack as "fresh snow", while in reality, an older snowpack is already present at the glacier and its surroundings. However, due to the expensiveness of the LES, a long spin-up period of e.g., weeks, is not feasible with our current set-up. We consider this possible shortcoming in our later analysis of the model data, and keep in mind that the modelled snowpack density profile likely differs from reality.

2.4.1 Snow drift module

155 A snow drift scheme based on the work of Sauter et al. (2013) was recently added to WRF by Schmid (2021). While the detailed description of the module and the implementation in WRF is subject to another paper (Sauter et al., 2023, in prep.), we outline the governing equations and most relevant features of the scheme in the following paragraphs.

The scheme builds on the widely-used approach of dividing the process of drifting snow into a saltation layer and snow particles in suspension. The saltation layer is fully parameterized and acts as a lower boundary condition for the flux of

160 snow into suspension. The drifting snow mainly interacts with the mean flow, while neglecting particle interactions. The mass conservation of snow particles is given by the continuity equation

$$\frac{\partial \phi_s}{\partial t} + \frac{\partial (\phi_s u_i)}{\partial x_i} = \frac{\partial}{\partial x_3}\left(\nu_t \frac{\partial \phi_s}{\partial x_3} - V\phi_s\right) + \left(\frac{\partial \phi_s}{\partial t}\right)_{sub}, \tag{1}$$

where ϕ_s is the mass concentration of snow particles in the suspension layer, $\partial \phi_s / \partial t$ is the local rate of snow concentration change, x_i are the Cartesian coordinates, u_i are the Cartesian components of the velocity vector, ν_t is the turbulent viscosity,

and V is the terminal fallout velocity. The fallout velocity

$$V(z) = -\frac{A}{r(z)}\sqrt{\left(\frac{A}{r(z)}\right)^2 + B \cdot r(z)}, \tag{2}$$

depends on the snow particle radius at height z

$$r(z) = r_0 \cdot z^{-0.258}, \tag{3}$$

A and B are constants and are calculated with:

$$A = \frac{6.203 \cdot \nu_{air}}{2} \tag{4}$$

and

$$B = \frac{5.516 \cdot \rho_{ice}}{4 \cdot \rho_{ice}} \cdot g. \tag{5}$$

Here ν_{air} represents the viscosity of air, ρ_{ice} the ice density and g the acceleration due to gravity.

r_0 is the particle radius at ground level following (Gordon et al., 2010) with:

$$r_0 = 0.5\left(\frac{7.8 \cdot 10^{-6} u_\star}{0.036} + 31 \cdot 10^{-6}\right), \tag{6}$$

and $u_\star$ the friction velocity. Optionally, $V(z)$ and r_0 can be set to constant values in the model settings.

The last term in Equation 1 accounts for the mass loss of suspended snow due to sublimation, where sublimation-loss rate of suspended snow is approximated by $\psi_s \phi_s$, with ψ_s as the sublimation-loss rate coefficient. This coefficient describes the change of snow particle mass due to heat exchange, and ventilation effects. The scheme considers the effect of sublimation on the vertical temperature and humidity profiles in the boundary layer. This feedback mechanism self-limits the sublimation process, because its intensity depends on the saturation deficit of the atmospheric environment (Sauter et al., 2013).

In the saltation layer, snow mass concentration is gained by aerodynamic entrainment from the snowpack below. Snow transport occurs when the surface shear stress exceeds the cohesive bond of the particles. The erosional mass flux is therefore proportional to the excess surface shear stress

$$q_e = e_{salt}\rho_a\left(\left[(u_{th} - u_*)\left(\frac{\phi_{salt}}{\phi_{max}}\right)^2 + u_*\right]^2 - u_{th}^2\right), \tag{7}$$

where ρ_a is the air density, u_* the surface shear stress, ϕ_{salt} the concentration in the saltation layer, u_{th} the friction threshold velocity, and ϕ_{max} the maximum particle concentration in the saltation layer. Since the particle erosion process depends on

the cohesive bonds of the snow particles, the surface shear stress threshold is a function of the snow density ρ_s (Walter et al., 2004):

$$u_{th} = 0.0195 + (0.021\sqrt{\rho_s}). \tag{8}$$

The efficiency of the erosion process is governed by the heuristic parameter e_{salt} [-]. Particle drag reduces the momentum, which in turn limits the capacity to eject further particles. When ϕ_{salt} reaches ϕ_{max}, the friction velocity reduces to the friction threshold velocity and the release of snow particles is stopped. The upper limit of ϕ_{max} is given by the semi-empirical relationship (Pomeroy and Male, 1992),

$$\phi_{max} = \frac{\rho_a}{3.29 \cdot u_*} \left(1 - \frac{u_{th}^2}{u_*^2} \right). \tag{9}$$

When the friction velocity drops below the threshold, particle deposition takes place. The deposition flux q_d corresponds to the downward flux and the modified shear stress ratio

$$q_d = V \phi_s \cdot \max \left(\frac{u_{th}^2 - u_*^2}{u_{th}^2}, 0 \right). \tag{10}$$

The first term on the right-hand side describes the vertical turbulent mixing of the snow and the terminal fall velocity V, while the second term shows the effect of sublimation in snow mass flux change.

3 Results

First, the observed snow depth changes from the TLS acquisitions are introduced and discussed in detail. In the next subsections, we explain the accompanying processes with the aid of further observations at point scale. We use the observations to evaluate the results from the LES, especially in terms of wind patterns and the resulting snow redistribution. Last, we compare the observed and modelled spatial patterns.

3.1 Observed snow depth changes with the TLS

The three TLS scans reveal the changes in snow depth over several days, and also show the heterogeneous snow distribution over the glacier and its surroundings. First, the DEM of Difference (DoD) between scan 1 and 2 shows an increase of surface elevation over almost the entire area of interest (Fig. 3a). The surface elevation increase is snowfall: the precipitation gauges at IHE and StHE registered precipitation, and the snow depth sensor at AWS28 observed a snow depth increase as well (Fig. 4). The snow was evenly distributed over the glacier surface, but the slopes adjacent to HEF showed a more heterogeneous snow distribution between scan 1 and 2 (Fig. 3a), which might indicate snow redistribution during the snow fall event. From the TLS data, 0.28 m of snow were deposited on average over the glacier and the snow depth sensor observed an increase of 0.45 m between scan 1 and 2 at AWS28. In this study, we do not elaborate on the snow depths at IHE and StHE, as the snow depth
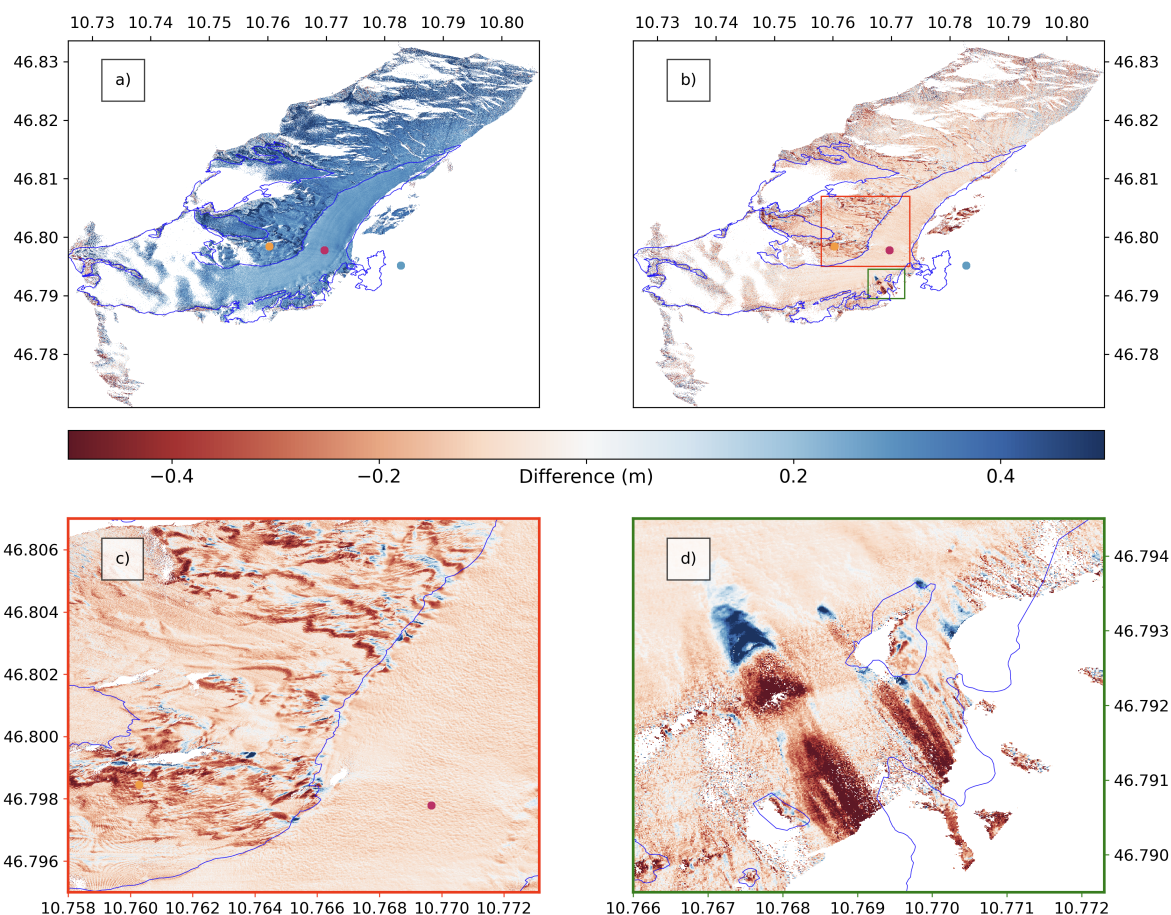
Figure 3. DEM of Difference of the TLS scans (Δx=1 m) between a) scan 1 and scan 2, and b) scan 2 and scan 3. c) is a zoom of the red box in b) showing signs of snow redistribution, and d) is a zoom of the green box in b) showing avalanches. The glacier outlines (blue) are derived from the ALS data acquired by the Federal Government of Tyrol in 2018. IHE (blue), StHE (orange), and AWS28 (pink) are also plotted.

215 sensors are installed at unrepresentative locations of the surroundings, i.e. at wind-exposed ridges that are almost never covered with snow.

The DoD between scan 2 and 3 shows a general decrease of the snow depth over the glacier of 0.079 m on average (Fig. 3b). This is in agreement with the snow depth observations at AWS28, where a decrease of 0.08 m was observed by the snow depth sensor between scan 2 and 3 (Fig. 4). A zoom in on the glacier surface on the orographic left side of the glacier (Fig. 3c) and a

220 look at the webcam images reveal patterns which are likely the results of snow redistribution, given their spatial structure. On the glacier surface around AWS28 (pink dot, Fig. 3c), a wavy pattern is evident with magnitudes between approximately -0.15 and -0.05 m. This is comparable to snow bedform observations over similar flat surfaces (Filhol and Sturm, 2015; Kochanski et al., 2018). With the resolution of the snow structure at Δx=1 m and the webcam images, we cannot distinguish between the snow bedforms (i.e. waves, dunes, barchans or ripples), but the structure is wind-driven. At the slopes adjacent to the glacier

225 surface, snow erosion is observed at the windward southwest slopes and this snow is deposited directly at the closest northeast leeward slopes. This is particularly evident around the location of StHE and the orographic left side of HEF (Fig. 3c). These structures are mainly induced by the rough surface caused by rocks at the slopes surrounding the glacier and again, indicate wind-driven snow.

230 Avalanches, induced by fresh snow or wind slabs, are observed over the orographic right side of HEF at an altitude of 2910 m a.s.l. (Fig. 3d). The release zone of the avalanche with magnitudes between -0.25 and -0.68 m is indicated by the dark red color, whereas the dark blue zone shows the deposition area of the avalanche up to +1.26 m high.

We here elaborated on the elevation changes at the glacier and the surroundings from the TLS observations, but we aim

235 to investigate the nature of these changes. The surface elevation changes are caused by redistributed snow, compaction and sublimation. Melt can be excluded during the cold case study period. To distinguish between these processes, we now analyse the additional meteorological observations and the numerical simulations with the WRF model.

3.2 Meteorological situation at the glacier

3.2.1 Precipitation

240 Mostly small precipitation amounts were registered on 5 and 6 Feb at StHE (Fig. 4). The situation changed when the front approached our area of interest. Webcam images, the precipitation gauge, and the increasing snow depth at AWS28 suggested that fresh snow was accumulated on 7 and 8 Feb. The last precipitation was registered at 06 UTC on 8 Feb. Precipitation was also registered during the acquisition of scan 1 and 3, but this precipitation was not evident in the TLS data and on the webcam images. For scan 1, the precipitation was actually registered after the TLS acquisition, as seen in the 10-min data. For scan 3, we

245 speculate that this is snow drift that is captured by the precipitation gauge. Snow redistribution patterns can only be simulated correctly if the modelled precipitation and wind patterns agree with the observations. In agreement with the observations (Fig. 4), the model simulates precipitation until 06 UTC (Fig. 6). We omit a direct comparison of the precipitations amounts at the precipitation gauge and the model, as precipitation observations are subject to undercatch, which is a well-known problem for precipitation (Goodison et al., 1998; Rasmussen et al., 2012; Smith, 2007; Colli et al., 2014). The data of the precipitation
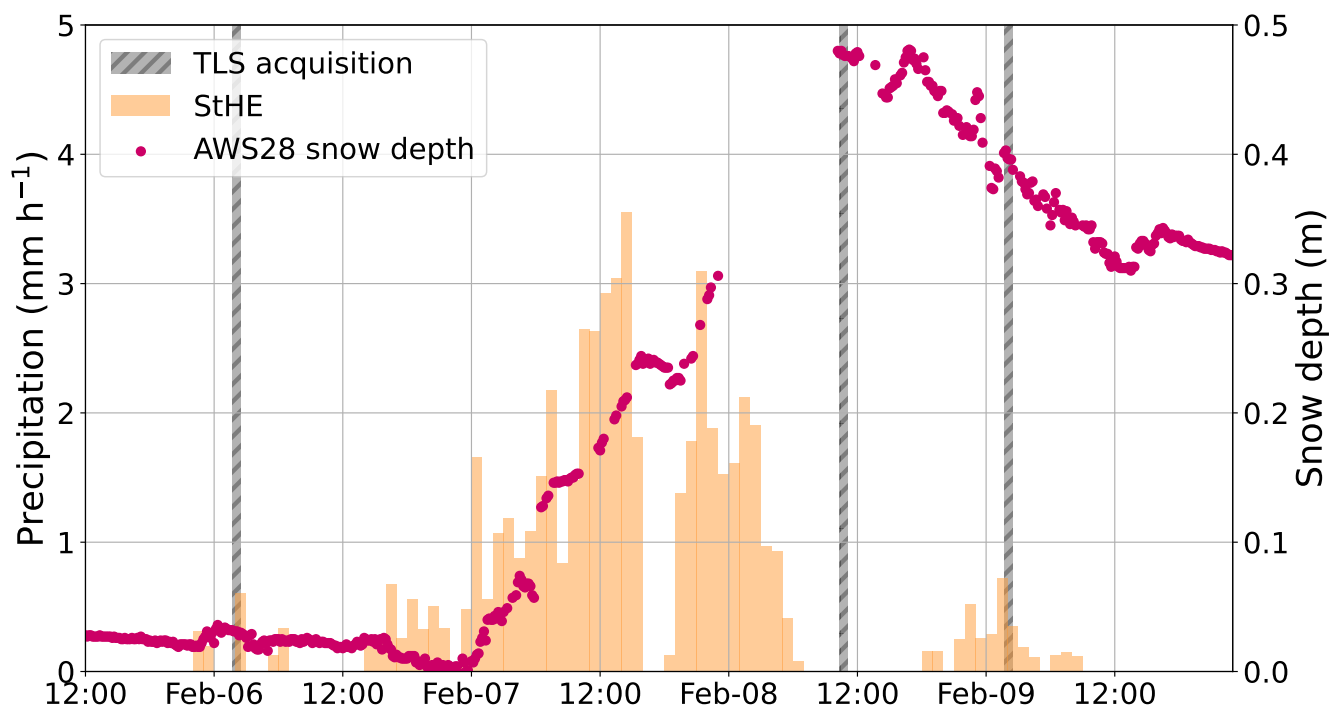
Figure 4. Precipitation (StHE: orange) and relative snow depth observations (AWS28: pink) during the case study period. Note that the precipitation observation is not corrected for undercatch and the snow depth is arbitrarily chosen to start at 0 m at the minimum observed during the case study period, despite the glacier was already covered in snow and thus, the actual snow depth was more than 0 m. The grey bars indicate the time of the TLS acquisitions.

250   gauge at IHE is not analysed here, as the gauge is placed at a wind-exposed ridge that is hardly ever covered with snow and is thus prone to large amounts of undercatch. The timing and registration of snowfall support the assumption that the snow depth increase between scan 1 and scan 2 (Fig. 3a) was due to solid precipitation.
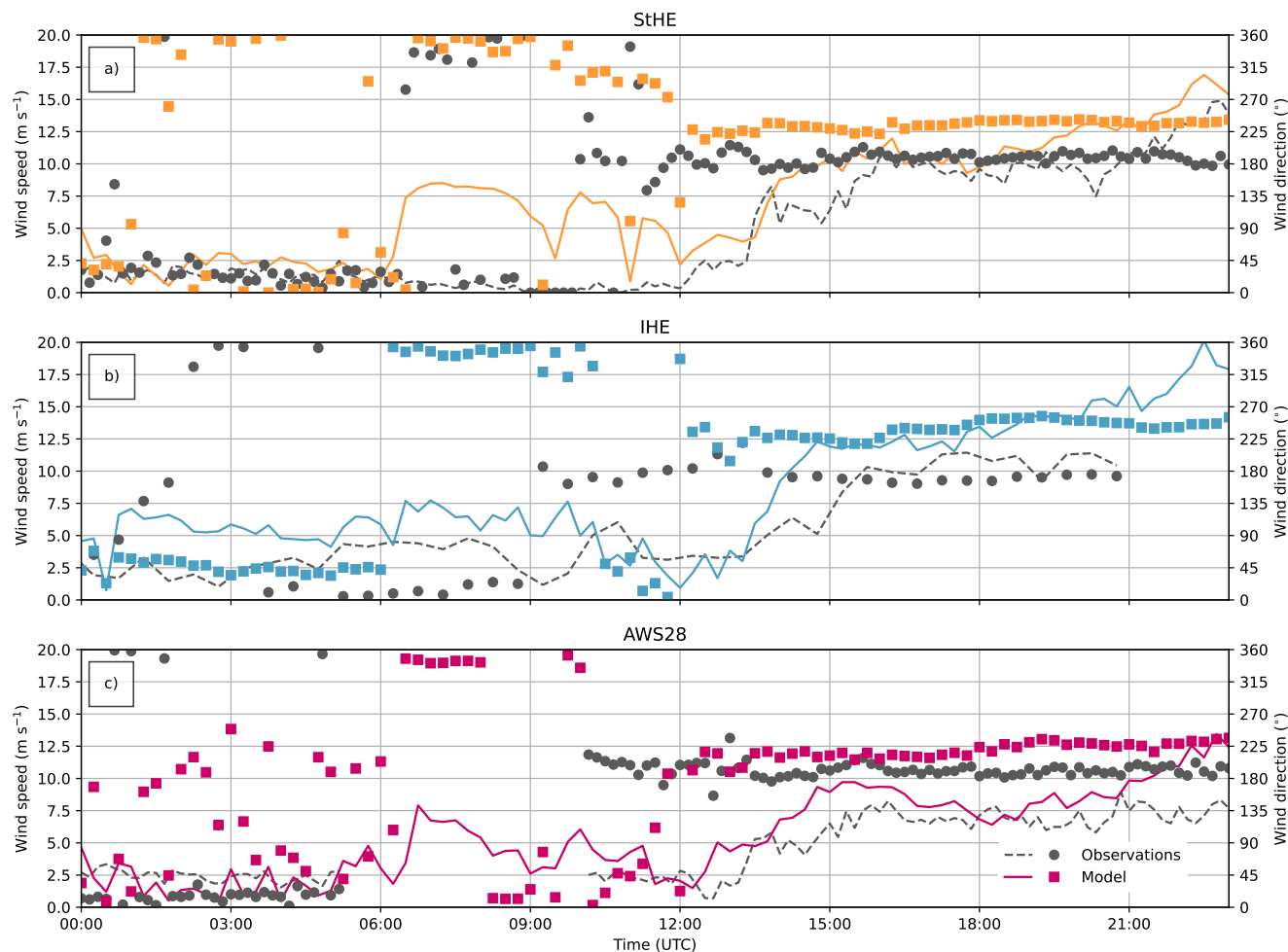
Figure 5. Time series of observations (grey) from the three weather stations and corresponding model output from the closest grid point in the model (IHE: blue; StHE: orange; AWS28: pink) of wind speed (lines) and wind direction (dots/squares) at 8 Feb 2021. Missing values in the observations are at IHE from 21:00 UTC onward, and at AWS28 between 05:45 UTC and 11:00 UTC.

3.2.2 Wind speed and direction

Observed time series of the wind speed and wind direction reveal the meteorological situation at the glacier and its surroundings
255 on 8 Feb (Fig. 5). All stations observed low wind speeds (less than 5 m s^{-1}) with mainly northerly flow during the night and the morning hours (8 Feb, 00 UTC–09 UTC). The wind direction changed towards southwesterly at around 09 UTC, while wind speed increased to more than 5 m s^{-1}. The wind speed increased even to more than 10 m s^{-1} at the south-facing slope (StHE) and the crest (IHE), while the wind speeds on the glacier remained below 10 m s^{-1}. After 15 UTC, higher wind speeds (more than 10 m s^{-1}) allowed for wind-driven snow distribution. Similar to the weather station observations, the model simulates low

260 wind speeds during the nighttime. However, the sudden increase in wind speed sets in an hour earlier than in the observations (Fig. 5). Furthermore, the wind direction deviated slightly (below 30°) from the observations throughout the simulations. Both the observations and the model suggest dominating southwesterly wind directions with wind speeds over $5\,\mathrm{m\,s^{-1}}$ at all three stations after 8 Feb, 12 UTC. This agrees with the TLS observations (Fig. 3c), which also indicate snow redistribution due to these strong, southwesterly winds. Overall, the model simulates the wind field on the glacier and the surrounding with

265 confidence and provides good input conditions for the snow redistribution and snow water equivalent (SWE) estimates.

3.2.3 Snow Water Equivalent, compaction and snow redistribution at point scale

The TLS observations do not give information on the individual contributions of redistributed snow, sublimation, and compaction to surface elevation changes. Compaction of snow can be detected, if the SWE remains constant after a snow fall event together with a simultaneous, continuous decrease in snow depth. SWE observations are not available during the case study

270 period, but to investigate the possible amounts of compaction at HEF, we had a look at data from an AWS that was installed at HEF in the winters of 2021/22 and 2022/23 at an altitude 3030 m a.s.l and provides SWE and snow depth data (Schröder, 2023). In these two winters, we examined snow depth and SWE data of nine snow fall events with amounts between 0.14 m and 0.38 m of fresh snow at the AWS. 16 hours after the snow fall, the snowpack decreased between -6.5% and -25% of the respective fresh snow amounts. In the mean time, no significant changes in the SWE were observed. Even though the winters

275 are not directly comparable (i.e.,the winter of of 2021/22 had extremely low precipitation amounts (Voordendag et al., 2023b)), the order of magnitude of compaction indicated that this process also likely occurred between scan 2 and 3 in February 2021. Furthermore, similar amounts of compaction are observed on other glaciers and snowpacks (Gugerli et al., 2019; Koch et al., 2019; Voordendag et al., 2021a). When we apply the compaction rates to the 0.28 m of fresh snow in the case study period, we find that between 0.018 m and 0.071 m of the surface elevation decrease can likely be attributed to compaction.

280 We now utilize the model output for further process understanding with a *qualitative* analysis of the modelled snowpack. This allows us to understand possible processes governing snowpack formation; therefore we start with snow redistribution at point scale. In the model, snow redistribution only occurs when the parameterised friction threshold velocity is exceeded by the current friction velocity. This value depends on the snow density (Eq. 8). Snow drift and subsequent redistribution is therefore only simulated after the increase of the wind speed to more than $10\,\mathrm{m\,s^{-2}}$ after 14 UTC. The simulated snow redistribution is

285 found to be 0.022 m at IHE, 0.014 at StHE, and 0.003 m at AWS28 at the end of the simulation period (Fig. 6a). The differences between the weather stations is directly related to the higher wind speeds at IHE and StHE than on the glacier at AWS28 (Fig. 5). Furthermore, it is interesting to note that the onset of snow drift initially leads to mass loss at all stations, at AWS28, however, snow drift briefly accumulates snow again after 18 UTC, while at the end of the simulation, the overall effects of snow drift is mass loss. At the other two stations (StHE and IHE), snow drift continuously contributes to snow mass loss.

290

Simulated changes in SWE give more insights on mass changes in the snowpack. During the precipitation event at the beginning of the simulation, the simulated SWE also increases, with similar values for IHE and StHE, but with about $0.4\,\mathrm{kg\,m^{-2}}$ higher values of SWE at AWS28 (Fig 6b). After snowfall ended and before snow drift started, the SWE values remain constant
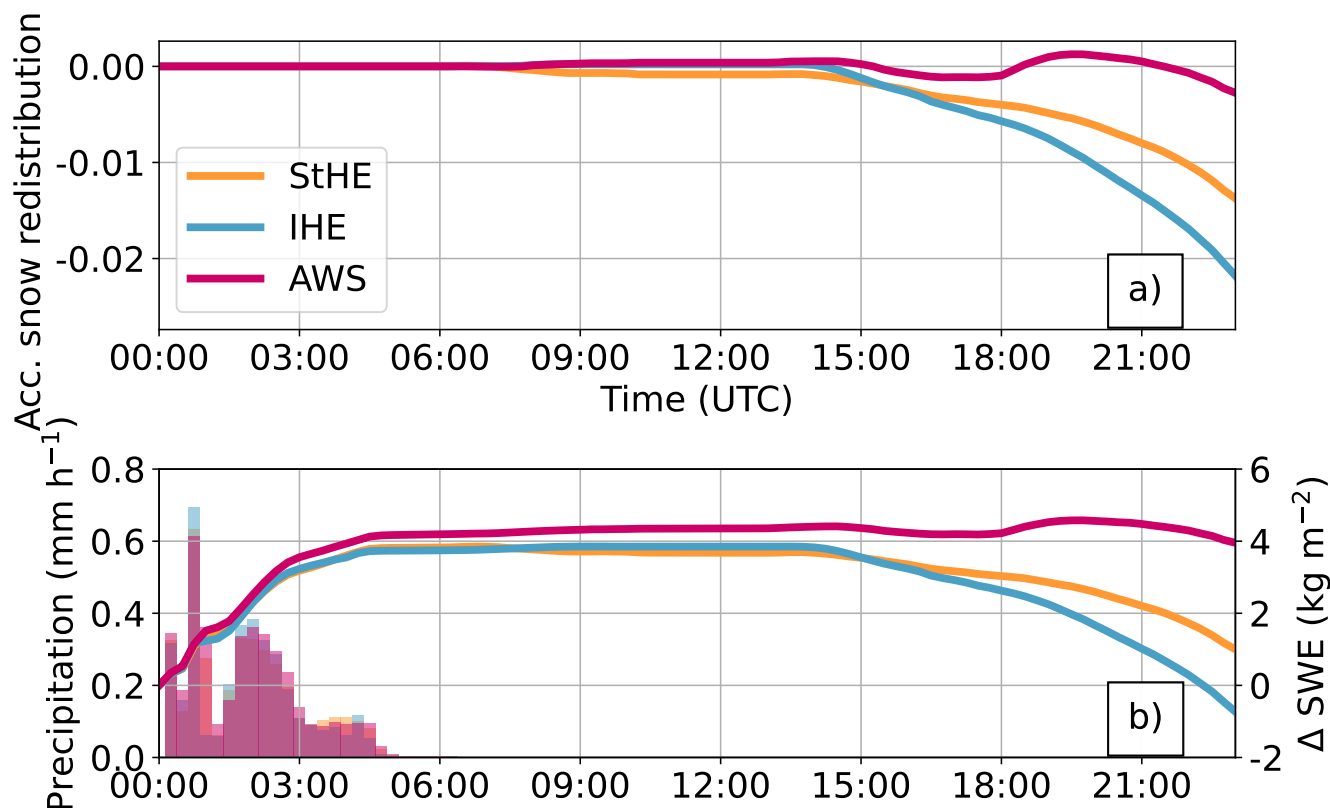
Figure 6. Time series at 8 Feb 2021 from the closest grid point in the model to StHE (orange), IHE (blue), and AWS28 (pink) in panel a) of accumulated snow redistribution (relative to the start of the simulation at 00 UTC), and panel b) solid precipitation (bars), and the relative change of snow water equivalent (Δ SWE, lines).

for the three stations, indicating that the surface elevation change during this period (Fig. 4) is snow compaction. As soon as
295   snow drift started, SWE reduces as snow gets eroded at the locations of the stations, but with spatial differences between IHE, StHE and AWS28 (Fig 6). The ridge location IHE exhibits the biggest reduction in SWE due to its exposed location over the entire simulation time. AWS28, however, shows a smaller total loss of SWE, mainly because of the sheltered location of the glacier. To summarize, SWE increased until 06 UTC due to solid precipitation, while SWE remained constant until 15 UTC due to compaction, until snow redistribution led to a continuous decrease in SWE after 15 UTC at all station.

300   Higher wind speeds result in more snow particles in the air and a higher likeliness of sublimation. Along with that, sublimation also depends on the vapor pressure in the ambient air as well as on the snow particle size. However, the values of simulated sublimation remain very small (less than 1 kg at the end of simulation for the entire air column over all glaciated areas in Fig. 1) throughout the rest of the simulation (not shown). Therefore, we will not discuss this process in more detail, also because the sublimation contribution is much smaller than the uncertainty of the TLS.

305 To summarize, during the precipitation phase, the SWE increases, while SWE mostly remains constant between 05 UTC and
14 UTC, and thereafter snow drift starts to erode mass.

3.3 Spatial patterns of simulated snow redistribution processes

To explore the spatial patterns beyond the point scale, we analyse the modeled snow redistribution relative to the start of the
simulation at 8 Feb, 00 UTC on the glacier and its surroundings (Fig. 7). The wind arrows reveal southwesterly flow at HEF
310 and its surroundings with wind speeds over $5\,\mathrm{m\,s^{-1}}$ when snow redistribution occurred. The simulated flow patterns were,
in agreement with the observations, almost perfectly down-glacier (Fig. 5). In the model, the governing process for snow
redistribution is erosion (Fig. 7a-d), which was especially strong at the mountain ridge northwest of HEF. This is in accordance
with the webcam images, which suggested that snow erosion mainly occurred at the surrounding mountain ridges. Snow
deposition (Fig. 7e-h), however, was very small compared to erosion and does not exceed 0.01 m after 24 hours of simulation
315 time. Therefore, the final snow redistribution (Fig. 7i-l) in the model is mainly governed by erosion, but some areas on leeward
slopes get more deposition than erosion (Fig. 7l, i.e. around coordinates 46.795°N, 10.82°W). At the end of the simulation,
the model suggests that around 0.09 m of snow were eroded at the mountain ridges, while at the glacier 0.03 m of snow were
eroded. Although there was a weak positive signal in snow redistribution in the vicinity of AWS28 at 15 UTC (Fig. 6 and 7i),
the sum of erosion and deposition resulted in an overall decrease in snow cover on the glacier. A main reason for this were
320 the rather high wind speeds throughout the domain, as in the observations, wind speeds reach up to $10\,\mathrm{m\,s^{-1}}$ after 15 UTC,
therefore snow can be easily eroded and transported towards the North-East and out of the domain.
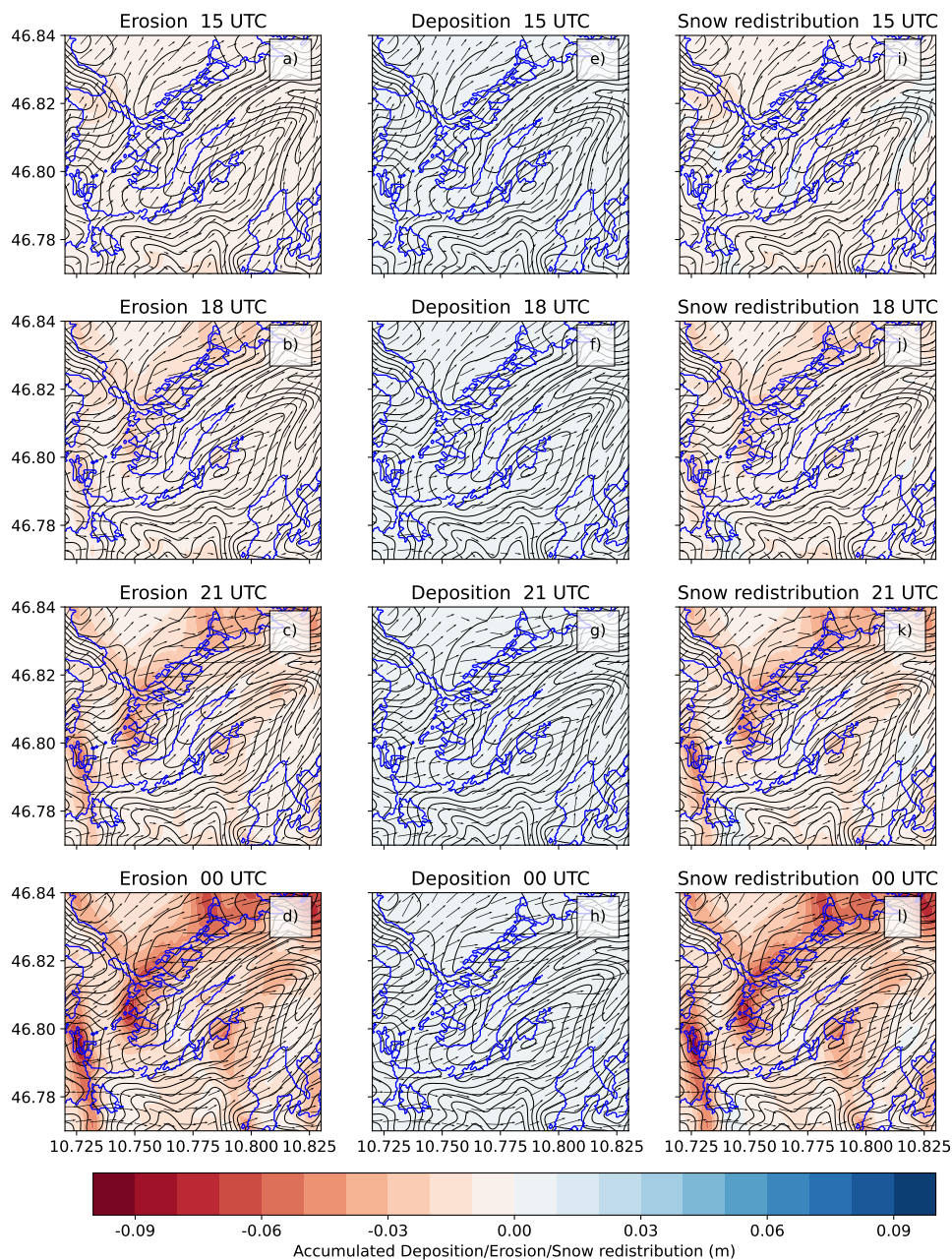
Figure 7. Simulated snow erosion (panels a-d), snow deposition (panels e-h) and the resulting net snow redistribution (panels i-l) in colors from 15 UTC, 18 UTC, 21 UTC and 00 UTC. Note that all values related to snow redistribution are summed up from simulation start (8 Feb, 00 UTC). Horizontal near surface wind speed and direction are indicated by black arrows. The black contours of 100 m equidistance show the model topography, blue contours indicate the glacier outlines.
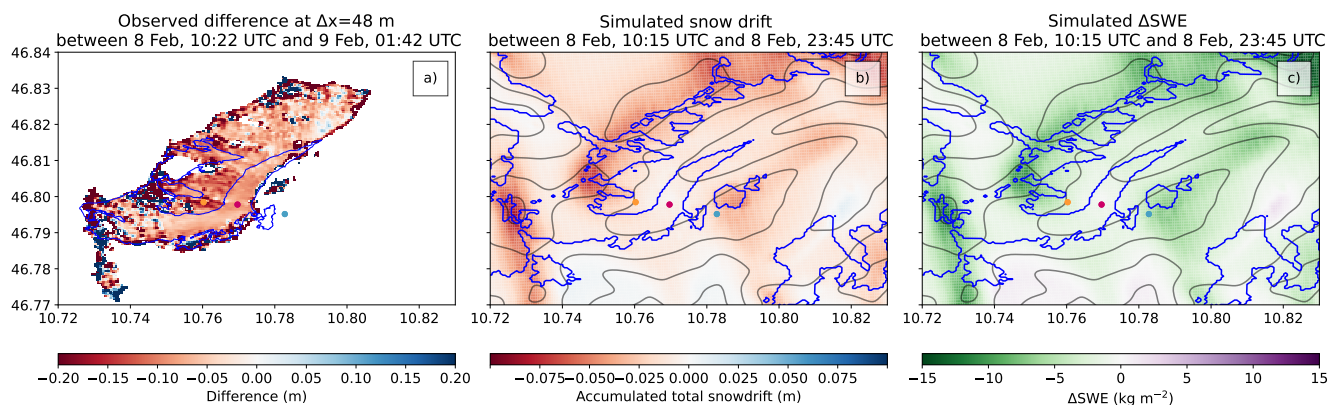
Figure 8. a) Observed snow depth changes over HEF at $\Delta x=48$ m between 8 Feb, 10:22 UTC and 9 Feb, 01:42 UTC, and b) the simulated snow redistribution and c) the simulated change in SWE between 8 Feb, 10:15 UTC and 9 Feb, 00:00 UTC. Please note the different orders of magnitude in a) and b).

3.4 Comparison of Observations with Simulations

A similar snow redistribution pattern as in the model also appears in the snow depth change observations by the TLS calculated to the model grid size of $\Delta x=48$ m between scan 2 and 3 (Fig. 8a). However, we compare the snow depth changes from the observations (between 8 Feb, 10:22 UTC and 9 Feb, 01:42 UTC) to the simulated snow redistribution (between 8 Feb, 10:15 UTC and 9 Feb, 00:00 UTC, Fig. 8b). We compare these different variables and see that the order of magnitude of the snow depth changes is twice as large as the simulated snow redistribution due to snow drift, because the observed snow depth changes also include compaction. The average simulated decrease caused by snow redistribution is 0.026 m over the glacier (Fig. 8b), which equals a decrease in SWE of -3.9 kg m^{-2} (Fig. 8c) in the simulated period over HEF. Considering that the observed compaction is estimated to be between 0.018 and 0.071 m of the fresh snow (Sec. 3.2.3) and the total decrease in observed snow depth is 0.079 m, we conclude that this mass and the magnitude of the simulated snow redistribution of 0.026 m is realistic and the observed snow redistribution patterns are captured accurately in the simulations.

4 Discussion

The present study combines operational TLS observations for a case study to evaluate LES to detect snow redistribution on an Alpine glacier. Since this is a small-scale phenomenon, it pushes both observations and modelling towards their boundaries.

The observations with the permanent TLS station are worldwide unique. Other studies also investigated snow depth changes with TLS (e.g. Mendoza et al., 2020; Gabbud et al., 2015; Fey et al., 2019) or ALS (Helfricht et al., 2014; Grünewald and Lehning, 2011), but these studies mainly covered coarser temporal resolutions or only covered small parts of a glacier. We were able to capture snow fall and redistribution directly thereafter, but we also note that the TLS observations are at the limits

340 of the capabilities of the system, as the uncertainty of the TLS observations was estimated at ± 0.10 m in vertical direction with manual post-processing (Voordendag et al., 2023a). For this study, the scans were registered with manually selected tie objects, such as snow-free rocks and the walls of StHE. We assume, looking at the registration of the scans at these tie objects, that the registration is even better than the ± 0.10 m in vertical direction, and thus the snow depth change between scan 2 and 3 was measured reliably, in a agreements with observations from the snow depth sensor at the glacier.

345 Modelling small-scale boundary-layer processes over mountainous topography is still a challenge for a NWP model like WRF, as discussed in the previous "summer study" by Goger et al. (2022). However, compared to the summer study, the model simulated even more realistic wind patterns over the glacier and its surroundings. Therefore, we assume that no model bias emerges due to erratic wind patterns. The simulated snow redistribution is realistic in terms of spatial structure and magnitude. Also, the simulated spatial patterns are very "smooth" compared to the TLS acquisitions. This is due to the smoothed model topography

350 restricted by numerical stability and therefore no exceeding slope angles over $35°$ – the model topography clearly deviates from real topography. The simulations show that snow is eroded mostly at the ridges and the glacier is sheltered as observed in nature. We note that simulated deposition is very small compared to the simulated erosion. High wind speeds immediately redistribute freshly deposited snow again, until it is transported out of the domain, therefore, erosion strongly dominates. Also, the very small-scale snow redistribution areas (Fig. 3c) cannot be captured at a Δx=48 m, since Mott and Lehning (2010)

355 noted that Δx=10 m or less would necessary to calculate the small-scale deposition patterns we observed with the TLS on the glacier. Still, we assume that the general snow redistribution patterns are well-simulated, as the model captures the larger snow redistribution at the mountain ridges and smaller snow redistribution and lower wind speeds at the less exposed parts of the glacier in agreements with weather station and TLS observations.

One of the advantages of the presented snow drift module in WRF is its sole simplicity compared to fully coupled atmospheric

360 and snow models (Vionnet et al., 2013; Sharma et al., 2023). The snow drift module is embedded within the WRF code and the land-surface scheme NOAH-MP, respectively. Nevertheless, the NOAH-MP provides only three layers in the snowpack, whereas physical multi-layer snow models, such as SNOWPACK (Lehning et al., 1999) or COSIPY (Sauter et al., 2020), are able to simulate more layers and thus have a better representation of the processes in the snowpack. However, with the aim to investigate the contribution of snow redistribution, it is only necessary to calculate the surface shear stress u_{th} (Eq. 8) depending

365 on the snow density of the upper layer in our snow drift module. However, the initialisation of the snowpack in our simulation is not comparable to nature, as the inner domain of the model is initialised with fresh snow only. The computationally expensive LES cannot be run with a long spin-up time to initialise the snowpack correctly. Thus, the model lacks of accurate information on the long-term snowpack evolution: In nature, the lower layers of the snow are compressed, but the upper layer with fresh snow is still uncompressed. It is more likely that snow drift takes place on an uncompressed, fresh snowpack rather than on a

370 dense snowpack. However, we consider this unproblematic for the simulation, as in both nature and simulation only the fresh snow is eroded. In the model, snow compaction is calculated following Anderson (1976). The results of this snow compaction (not shown) are overestimated, because the model assumes the entire snowpack (>2 m) to compact and not only the 0.48 m of fresh snow. To conclude, we found realistic amounts of snow redistribution with our simulated results, we therefore conclude

that a three-layer model for the snowpack is sufficient to qualitatively assess wind-driven snow redistribution.

375

In general, snow redistribution contributes to the glacier mass balance (Dadic et al., 2010) and for this specific case study, snow redistribution has a negative effect on the glacier mass balance. In the simulation $-3.9\,\mathrm{kg\,m^{-2}}$ of snow is blown away from the glacier and out of the domain in the simulated period. We only focused on one case study, as the period was characterized by low wind speeds during snow fall and increased in the period thereafter. Furthermore, during this period, AWS28 was

380 installed at the glacier and the second scan was taken directly after snow fall. It is clear that with this one "golden day" of snow redistribution on the glacier, we cannot attribute for the seasonal contribution of snow redistribution for the glacier mass balance. Further research is needed to investigate this seasonal contribution using our extensive TLS data set, preferably also to investigate snow redistribution patterns under different prevalent wind directions (e.g., Southerly or North-Westerly). Our study shows that a fresh snow fall event and a rapid increase in wind speeds directly thereafter are favorable conditions for snow drift

385 to occur; therefore, snow drift is likely to occur mostly in connection with frontal passages or downslope windstorms. Obleitner (1994) studied wind regimes at HEF and found a dominance of mostly thermally-induced circulations; however, an updated version of the wind climatology at the glacier would allow new insights on under which wind regimes snow redistribution could occur.

Finally, although the installation of a permanent TLS station in remote mountainous terrain is a logistical challenge, the WRF
390 model setup could be applied to any location worldwide. Therefore, our model setup can also be utilized for snow redistribution studies at other glaciated areas.

5 Conclusions

In this study, we introduced unique TLS scans to validate LES with the WRF model for quantifying the effect of snow redistribution over Hintereisferner, a major Alpine glacier in the Austrian Alps. For this purpose, we present a case study between 6 and

395 9 Feb, 2021, where multiple TLS scans and additional observations of wind speeds and snow depth on the glacier are available. Webcam imagery revealed snow drift in the area. With this rich observational data set, we evaluated large-eddy simulations at Δx=48 m with the WRF model including a newly implemented snowdrift module. Our major findings are summarized as follows:

- Surface elevation changes due to snow fall and snow redistribution are observed with the TLS between 6 Feb, 01:42 UTC
400 and 9 Feb, 01:42 UTC, 2021. Simulations were performed for 8 Feb, and run for 24 hours. The high-resolution setup in both observations and simulations at HEF is able to capture the glacier-wide snow redistribution patterns.

- Typical snow redistribution patterns are observed in the TLS scans. They show spatial heterogeneity, while on the glacier the patterns are less prominent than on the orographic left slope.

- Observations with the TLS show a glacier-wide spatially averaged decrease of 0.079 m of the snowpack the 15 hours
405 directly after the snow fall. This reduction of the snow depth is a combination between snow compaction and snow

redistribution. With the observations at hand, compaction and drift cannot be separated, but the estimated compaction of the snowpack decrease is between 6.5% and 25% of the fresh snow amount.

– The WRF model at Δx=48 m simulated the wind patterns at the glacier exceptionally well, and a newly implemented snow drift module allows a detailed comparison with the TLS acquisitions. The simulated integrated glacier-wide snow redistribution is on spatial average 0.026 m. The snow redistribution patterns are captured in a realistic manner compared to the observations.

– A qualitative inspection of the modelling results reveals that snow is mostly eroded on the surrounding mountain ridges, while the glacier itself is in a sheltered location and experiences less snow redistribution.

– Snow redistribution has a negative effect on the glacier mass balance in this case study with a simulated mass decrease of -3.9 kg m^{-2} in 24 h. However, the contribution of these snow amounts to the seasonal glacier mass balance remains illusive as this study only covers one case study with a specific wind pattern, but this is an opportunity for further research.

– The high-resolution observations with the permanent TLS are worldwide unique and therefore not directly transferable to other glaciers.

– The WRF model setup with the snow drift module can be applied to any other location in the world, when high-resolution static and meteorological input data are available for the location of interest.

This study highlights the impact of snow distribution over a major Alpine glacier. The set-up, at least on the modelling side, is "portable" to any other location in the world. Snow redistribution patterns depend on the wind field and the local topography; therefore, our work shows the potential impact of small-scale boundary layer processes on glaciers' mass balance.

Code availability. The snow drift module for WRF can be found in the following Github repository of Christina Schmid: https://github.com/ChristinaSchmid/snowdrift. The namelists for the LES simulations are available at https://github.com/gogerbr/wrf_les_hintereisferner

Author contributions. AV selected the case study period, and conducted and post-processed the TLS observations. BG conducted the WRF simulations and analyzed the model output. AV and BG wrote the original manuscript. RP oversaw the meteorological and mass balance observations at HEF. TS developed the snow drift module and implemented it with CS into the model code, while the code is currently maintained by MS. GK, TM, and TS conceived the project idea and oversaw the entire progress of the project. All authors contributed to the manuscript and improved it where necessary.

Competing interests. Tobias Sauter and Thomas Mölg are members of the editorial board of TC.

Acknowledgements. This work is part of the project "Measuring and modeling snow-cover dynamics at high resolution for improving distributed mass balance research on mountain glaciers", a joint project fully funded by the Austrian Science Foundation (FWF; project number I 3841-N32) and the Deutsche Forschungsgemeinschaft (DFG; project number SA 2339/7-1). The computational results presented have been achieved using the Vienna Scientific Cluster (VSC) under project number 71434. We would like to thank Wolfgang Gurgiser and Philipp Vettori for their assistance in installing weather stations on and around HEF. Christian Georges, Christoph Klug and Rudolf Sailer facilitated the TLS setup.

References

440   Anderson, E. A.: A point energy and mass balance model of a snow cover., Stanford University, 1976.

Arduini, G., Balsamo, G., Dutra, E., Day, J. J., Sandu, I., Boussetta, S., and Haiden, T.: Impact of a Multi-Layer Snow Scheme on Near-Surface Weather Forecasts, J. Adv. Model. Earth Sys., 11, 4687–4710, https://doi.org/https://doi.org/10.1029/2019MS001725, 2019.

Beniston, M., Farinotti, D., Stoffel, M., Andreassen, L. M., Coppola, E., Eckert, N., Fantini, A., Giacona, F., Hauck, C., Huss, M., Huwald, H., Lehning, M., López-Moreno, J.-I., Magnusson, J., Marty, C., Morán-Tejéda, E., Morin, S., Naaim, M., Provenzale, A., Rabatel, A.,

445   Six, D., Stötter, J., Strasser, U., Terzago, S., and Vincent, C.: The European mountain cryosphere: a review of its current state, trends, and future challenges, The Cryosphere, 12, 759–794, https://doi.org/10.5194/tc-12-759-2018, 2018.

Blümcke, A. and Hess, H.: Untersuchungen am Hintereisferner, Zeitschrift des deutschen und österreichischen Alpenvereins, https://opac.geologie.ac.at/ais312/dokumente/AV_001_2.pdf, 1899.

Cogley, J. G., Hock, R., Rasmussen, L., Arendt, A., Bauder, A., Braithwaite, R., Jansson, P., Kaser, G., Möller, M., Nicholson, L., and Zemp,

450   M.: Glossary of glacier mass balance and related terms, IHP-VII technical documents in hydrology, 86, 2011.

Colle, B. A., Smith, R. B., and Wesley, D. A.: Theory, Observations, and Predictions of Orographic Precipitation, in: Mountain Weather Research and Forecasting, edited by Chow, F. K., De Wekker, S. F. J., and Snyder, B. J., Springer Atmospheric Sciences, pp. 291–344, Springer Netherlands, https://doi.org/10.1007/978-94-007-4098-3_6, 2013.

Colli, M., Lanza, L., Barbera, P. L., and Chan, P.: Measurement accuracy of weighing and tipping-bucket rainfall intensity gauges under

455   dynamic laboratory testing, Atmos. Res., 144, 186–194, https://doi.org/10.1016/j.atmosres.2013.08.007, 2014.

Copernicus Climate Change Service (C3S): European State of the Climate 2022, https://doi.org/10.24381/GVAF-H066, 2023.

Cremona, A., Huss, M., Landmann, J. M., Borner, J., and Farinotti, D.: European heat waves 2022: contribution to extreme glacier melt in Switzerland inferred from automated ablation readings, The Cryosphere, 17, 1895–1912, https://doi.org/10.5194/tc-17-1895-2023, 2023.

Dadic, R., Mott, R., Lehning, M., and Burlando, P.: Wind influence on snow depth distribution and accumulation over glaciers, J Geophys

460   Res: Earth Surface, 115, https://doi.org/10.1029/2009JF001261, 2010.

Deardorff, J. W.: Stratocumulus-capped mixed layers derived from a three-dimensional model, Boundary-Layer Meteorol., 18, 495–527, https://doi.org/10.1007/BF00119502, 1980.

European Environmental Agency: Copernicus Land Service — Pan-European Component: CORINE Land Cover, http://land.copernicus.eu/pan-european/corine-land-cover/clc-2012, 2017.

465   Fey, C., Schattan, P., Helfricht, K., and Schöber, J.: A compilation of multitemporal TLS snow depth distribution maps at the Weisssee snow research site (Kaunertal, Austria), Water Resour. Res., https://doi.org/10.1029/2019wr024788, 2019.

Filhol, S. and Sturm, M.: Snow bedforms: A review, new data, and a formation model, Journal of Geophysical Research: Earth Surface, 120, 1645–1669, https://doi.org/10.1002/2015jf003529, 2015.

Fischer, M., Huss, M., Kummert, M., and Hoelzle, M.: Application and validation of long-range terrestrial laser scanning to monitor the mass

470   balance of very small glaciers in the Swiss Alps, The Cryosphere, 10, 1279–1295, https://doi.org/10.5194/tc-10-1279-2016, 2016.

Fox-Kemper, B., Hewitt, H., Xiao, C., Aðalgeirsdóttir, G., Drijfhout, S., Edwards, T., Golledge, N., Hemer, M., Kopp, R., Krinner, G., Mix, A., Notz, D., Nowicki, S., Nurhati, I., Ruiz, L., Sallée, J.-B., Slangen, A., and Yu, Y.: Climate Change 2021: The Physical Science Basis. Contribution of Working Group I to the Sixth Assessment Report of the Intergovernmental Panel on Climate Change, chap. Ocean, Cryosphere and Sea Level Change, p. 1211–1362, Cambridge University Press, 2021.

475 Frei, C. and Schär, C.: A precipitation climatology of the Alps from high-resolution rain-gauge observations, Int. J. Climatol., 18, 873–900, https://doi.org/10.1002/(SICI)1097-0088(19980630)18:8<873::AID-JOC255>3.0.CO;2-9, 1998.

Gabbud, C., Micheletti, N., and Lane, S. N.: Lidar measurement of surface melt for a temperate Alpine glacier at the seasonal and hourly scales, J. Glaciol., 61, 963–974, https://doi.org/10.3189/2015jog14j226, 2015.

Gerber, F., Lehning, M., Hoch, S. W., and Mott, R.: A close-ridge small-scale atmospheric flow field and its influence on snow accumulation,
480   J. Geophys. Res. Atmos., 122, 7737–7754, https://doi.org/10.1002/2016JD026258, 2017.

Gerber, F., Besic, N., Sharma, V., Mott, R., Daniels, M., Gabella, M., Berne, A., Germann, U., and Lehning, M.: Spatial variability in snow precipitation and accumulation in COSMO–WRF simulations and radar estimations over complex terrain, The Cryosphere, 12, 3137–3160, https://doi.org/10.5194/tc-12-3137-2018, 2018.

Goger, B., Rotach, M. W., Gohm, A., Fuhrer, O., Stiperski, I., and Holtslag, A. A. M.: The Impact of Three-Dimensional Effects on the
485   Simulation of Turbulence Kinetic Energy in a Major Alpine Valley, Boundary-Layer Meteorol, 168, 1–27, https://doi.org/10.1007/s10546-018-0341-y, 2018.

Goger, B., Rotach, M. W., Gohm, A., Stiperski, I., Fuhrer, O., and de Morsier, G.: A New Horizontal Length Scale for a Three-Dimensional Turbulence Parameterization in Mesoscale Atmospheric Modeling over Highly Complex Terrain, J. Appl. Meteor. Climatol., 58, 2087–2102, https://doi.org/10.1175/JAMC-D-18-0328.1, 2019.

490 Goger, B., Stiperski, I., Nicholson, L., and Sauter, T.: Large-eddy simulations of the atmospheric boundary layer over an Alpine glacier: Impact of synoptic flow direction and governing processes, Q. J. R. Meteorol. Soc, 148, 1319–1343, https://doi.org/10.1002/qj.4263, 2022.

Goodison, B. E., Louie, P. Y., and Yang, D.: WMO solid precipitation measurement intercomparison, World Meteorological Organization, 1998.

495 Gordon, M., Biswas, S., Taylor, P. A., Hanesiak, J., Albarran-Melzer, M., and Fargey, S.: Measurements of drifting and blowing snow at Iqaluit, Nunavut, Canada during the star project, Atmosphere-Ocean, 48, 81–100, https://doi.org/10.3137/AO1105.2010, 2010.

Grünewald, T. and Lehning, M.: Altitudinal dependency of snow amounts in two small alpine catchments: can catchment-wide snow amounts be estimated via single snow or precipitation stations?, Ann. of Glaciol., 52, 153–158, https://doi.org/10.3189/172756411797252248, 2011.

500 Grünewald, T., Bühler, Y., and Lehning, M.: Elevation dependency of mountain snow depth, The Cryosphere, 8, 2381–2394, https://doi.org/10.5194/tc-8-2381-2014, 2014.

Gugerli, R., Salzmann, N., Huss, M., and Desilets, D.: Continuous and autonomous snow water equivalent measurements by a cosmic ray sensor on an alpine glacier, The Cryosphere, 13, 3413–3434, https://doi.org/10.5194/tc-13-3413-2019, 2019.

Helfricht, K., Kuhn, M., Keuschnig, M., and Heilig, A.: Lidar snow cover studies on glaciers in the Ötztal Alps (Austria): comparison with
505   snow depths calculated from GPR measurements, The Cryosphere, 8, 41–57, https://doi.org/10.5194/tc-8-41-2014, 2014.

Hock, R., Rasul, G., Adler, C., Cáceres, B., Gruber, S., Hirabayashi, Y., Jackson, M., Kääb, A., Kang, S., Kutuzov, S., Milner, A., Molau, U., Morin, S., Orlove, B., and Steltzer, H.: High Mountain Areas, in: IPCC Special Report on the Ocean and Cryosphere in a Changing Climate, edited by Pörtner, H.-O., Roberts, D., Masson-Delmotte, V., Zhai, P., Tignor, M., Poloczanska, E., Mintenbeck, K., Alegría, A., Nicolai, M., Okem, A., Petzold, J., Rama, B., and Weyer, N., pp. 131–202, Cambridge University Press,
510   https://doi.org/10.1017/9781009157964.004, 2022.

Hugonnet, R., McNabb, R., Berthier, E., Menounos, B., Nuth, C., Girod, L., Farinotti, D., Huss, M., Dussaillant, I., Brun, F., and Kääb, A.: Accelerated global glacier mass loss in the early twenty-first century, Nature, 592, 726–731, https://doi.org/10.1038/s41586-021-03436-z, 2021.

Huss, M. and Hock, R.: Global-scale hydrological response to future glacier mass loss, Nature Climate Change, 8, 135–140, https://doi.org/10.1038/s41558-017-0049-x, 2018.

Iacono, M. J., Delamere, J. S., Mlawer, E. J., Shephard, M. W., Clough, S. A., and Collins, W. D.: Radiative forcing by long-lived greenhouse gases: Calculations with the AER radiative transfer models, J. Geophys. Res. Atmos., 113, https://doi.org/10.1029/2008JD009944, 2008.

Isotta, F. A., Frei, C., Weilguni, V., Perčec Tadić, M., Lassègues, P., Rudolf, B., Pavan, V., Cacciamani, C., Antolini, G., Ratto, S. M., Munari, M., Micheletti, S., Bonati, V., Lussana, C., Ronchi, C., Panettieri, E., Marigo, G., and Vertačnik, G.: The climate of daily precipitation in the Alps: development and analysis of a high-resolution grid dataset from pan-Alpine rain-gauge data, Int. J. Climatol., 34, 1657–1675, https://doi.org/https://doi.org/10.1002/joc.3794, 2013.

Jiménez, P. A., Dudhia, J., González-Rouco, J. F., Navarro, J., Montávez, J. P., and García-Bustamante, E.: A Revised Scheme for the WRF Surface Layer Formulation, Mon. Wea. Rev., 140, 898 – 918, https://doi.org/10.1175/MWR-D-11-00056.1, 2012.

Koch, F., Henkel, P., Appel, F., Schmid, L., Bach, H., Lamm, M., Prasch, M., Schweizer, J., and Mauser, W.: Retrieval of Snow Water Equivalent, Liquid Water Content, and Snow Height of Dry and Wet Snow by Combining GPS Signal Attenuation and Time Delay, Water Resour. Res., 55, 4465–4487, https://doi.org/10.1029/2018wr024431, 2019.

Kochanski, K., Anderson, R. S., and Tucker, G. E.: Statistical Classification of Self-Organized Snow Surfaces, Geophysical Research Letters, 45, 6532–6541, https://doi.org/10.1029/2018gl077616, 2018.

Lehning, M., Bartelt, P., Brown, B., Russi, T., Stöckli, U., and Zimmerli, M.: SNOWPACK model calculations for avalanche warning based upon a new network of weather and snow stations, Cold Reg. Sci. Technol., 30, 145–157, https://doi.org/10.1016/s0165-232x(99)00022-1, 1999.

Machguth, H., Paul, F., Hoelzle, M., and Haeberli, W.: Distributed glacier mass-balance modelling as an important component of modern multi-level glacier monitoring, Ann. Glaciol., 43, 335–343, https://doi.org/10.3189/172756406781812285, 2006.

Marzeion, B., Jarosch, A., and Hofer, M.: Past and future sea-level change from the surface mass balance of glaciers, The Cryosphere, 6, 1295, https://doi.org/10.5194/tc-6-1295-2012, 2012.

Mendoza, P. A., Shaw, T. E., McPhee, J., Musselman, K. N., Revuelto, J., and MacDonell, S.: Spatial Distribution and Scaling Properties of Lidar-Derived Snow Depth in the Extratropical Andes, Water Resour. Res., 56, https://doi.org/10.1029/2020wr028480, 2020.

Mott, R. and Lehning, M.: Meteorological Modeling of Very High-Resolution Wind Fields and Snow Deposition for Mountains, Journal of Hydrometeorology, 11, 934–949, https://doi.org/10.1175/2010jhm1216.1, 2010.

Mott, R., Vionnet, V., and Grünewald, T.: The Seasonal Snow Cover Dynamics: Review on Wind-Driven Coupling Processes, Front. Earth Sci., 6, 197, https://doi.org/10.3389/feart.2018.00197, 2018.

Nakanishi, M. and Niino, H.: Development of an Improved Turbulence Closure Model for the Atmospheric Boundary Layer, J. Meteor. Soc. Japan Ser. II, 87, 895–912, https://doi.org/10.2151/jmsj.87.895, 2009.

Niu, G.-Y., Yang, Z.-L., Mitchell, K. E., Chen, F., Ek, M. B., Barlage, M., Kumar, A., Manning, K., Niyogi, D., Rosero, E., Tewari, M., and Xia, Y.: The community Noah land surface model with multiparameterization options (Noah-MP): 1. Model description and evaluation with local-scale measurements, J. Geophys. Res. Atmos., 116, https://doi.org/10.1029/2010JD015139, 2011.

Obleitner, F.: Climatological features of glacier and valley winds at the Hintereisferner (Ötztal Alps, Austria), Theor. Appl. Climatol., 49, 225–239, https://doi.org/10.1007/BF00867462, 1994.

Pomeroy, J. and Male, D.: Steady-state suspension of snow, J. Hydrol., 136, 275–301, 1992.

550 Prantl, H., Nicholson, L., Sailer, R., Hanzer, F., Juen, I., and Rastner, P.: Glacier Snowline Determination from Terrestrial Laser Scanning Intensity Data, Geosciences, 7, 60, https://doi.org/10.3390/geosciences7030060, 2017.

Rasmussen, R., Baker, B., Kochendorfer, J., Meyers, T., Landolt, S., Fischer, A. P., Black, J., Thériault, J. M., Kucera, P., Gochis, D., Smith, C., Nitu, R., Hall, M., Ikeda, K., and Gutmann, E.: How Well Are We Measuring Snow: The NOAA/FAA/NCAR Winter Precipitation Test Bed, Bulletin of the American Meteorological Society, 93, 811–829, https://doi.org/10.1175/bams-d-11-00052.1, 2012.

555 RIEGL: RiSCAN PRO, RIEGL Laser Measurement Systems, Horn, Austria, 2.8.0 edn., 2019.

Rotach, M. W., Stiperski, I., Fuhrer, O., Goger, B., Gohm, A., Obleitner, F., Rau, G., Sfyri, E., and Vergeiner, J.: Investigating Exchange Processes over Complex Topography: The Innsbruck Box (i-Box), Bull. Amer. Meteor. Soc., 98, 787–805, https://doi.org/10.1175/BAMS-D-15-00246.1, 2017.

Sauter, T. and Galos, S. P.: Effects of local advection on the spatial sensible heat flux variation on a mountain glacier, The Cryosphere, 10, 560 2887–2905, https://doi.org/10.5194/tc-10-2887-2016, 2016.

Sauter, T., Möller, M., Finkelnburg, R., Grabiec, M., Scherer, D., and Schneider, C.: Snowdrift modelling for the Vestfonna ice cap, north-eastern Svalbard, The Cryosphere, 7, 1287–1301, https://doi.org/10.5194/tc-7-1287-2013, 2013.

Sauter, T., Arndt, A., and Schneider, C.: COSIPY v1.3 – an open-source coupled snowpack and ice surface energy and mass balance model, Geosci. Model Dev., 13, 5645–5662, https://doi.org/10.5194/gmd-13-5645-2020, 2020.

565 Sauter, T., Saigger, M., Schmid, C., Collier, E., Goger, B., Kaser, G., Prinz, R., Voordendag, A. B., and Mölg, T.: Snowdrift scheme in the Weather Research and Forecasting model, in preparation, 2023.

Schmid, C.: Implementierung eines Schneedriftmoduls in das Weather Research and Forecasting (WRF) Modell und eine erste Evaluation, Ph.D. thesis, Friedrich-Alexander-Universität Erlangen-Nürnberg (FAU), https://opus4.kobv.de/opus4-fau/frontdoor/index/index/docId/17236, 2021.

570 Schröder, M.: Snow Water Equivalent measured by a Cosmic Ray Neutron Sensor: A Case Study from Hintereisferner (Austria), Master's thesis, Universität Innsbruck, in preparation, 2023.

Sharma, V., Gerber, F., and Lehning, M.: Introducing CRYOWRF v1.0: multiscale atmospheric flow simulations with advanced snow cover modelling, Geosci. Model Dev., 16, 719–749, https://doi.org/10.5194/gmd-16-719-2023, 2023.

Skamarock, W. C., Klemp, J. B., Dudhia, J., Gill, D. O., Liu, Z., Berner, J., Wang, W., Powers, J. G., Duda, M. G., Barker, D. M., and 575 Huang, X.-Y.: A Description of the Advanced Research WRF Model Version 4, Tech. rep., NCAR Technical Note NCAR/TN-556+STR, https://doi.org/10.5065/1dfh-6p97, 2019.

Smith, C. D.: Correcting the wind bias in snowfall measurements made with a Geonor T-200B precipitation gauge and alter wind shield, Proceedings of the 14th SMOI, San Antonio, 20, 2007.

Stiperski, I. and Rotach, M. W.: On the Measurement of Turbulence Over Complex Mountainous Terrain, Boundary-Layer Meteorol., 159, 580 97–121, https://doi.org/10.1007/s10546-015-0103-z, 2016.

Strasser, U., Marke, T., Braun, L., Escher-Vetter, H., Juen, I., Kuhn, M., Maussion, F., Mayer, C., Nicholson, L., Niedertscheider, K., Sailer, R., Stötter, J., Weber, M., and Kaser, G.: The Rofental: a high Alpine research basin (1890–3770 m a.s.l.) in the Ötztal Alps (Austria) with over 150 years of hydrometeorological and glaciological observations, Earth Syst. Sci. Data, 10, 151–171, https://doi.org/10.5194/essd-10-151-2018, 2018.

585 Thompson, G., Field, P. R., Rasmussen, R. M., and Hall, W. D.: Explicit Forecasts of Winter Precipitation Using an Improved Bulk Microphysics Scheme. Part II: Implementation of a New Snow Parameterization, Mon. Wea. Rev., 136, 5095 – 5115, https://doi.org/10.1175/2008MWR2387.1, 2008.

Umek, L., Gohm, A., Haid, M., Ward, H. C., and Rotach, M. W.: Large eddy simulation of foehn-cold pool interactions in the Inn Valley during PIANO IOP2, Q. J. R. Meteor. Soc., 147, 944–982, https://doi.org/10.1002/qj.3954, 2021.

590 Vionnet, V., Guyomarc'h, G., Bouvet, F. N., Martin, E., Durand, Y., Bellot, H., Bel, C., and Puglièse, P.: Occurrence of blowing snow events at an alpine site over a 10-year period: Observations and modelling, Adv. Water Resour., 55, 53 – 63, https://doi.org/10.1016/j.advwatres.2012.05.004, snow-Atmosphere Interactions and Hydrological Consequences, 2013.

Vionnet, V., Martin, E., Masson, V., Guyomarc'h, G., Naaim-Bouvet, F., Prokop, A., Durand, Y., and Lac, C.: Simulation of wind-induced snow transport and sublimation in alpine terrain using a fully coupled snowpack/atmosphere model, The Cryosphere, 8, 395–415, 595 https://doi.org/10.5194/tc-8-395-2014, 2014.

Vionnet, V., Dombrowski-Etchevers, I., Lafaysse, M., Quéno, L., Seity, Y., and Bazile, E.: Numerical Weather Forecasts at Kilometer Scale in the French Alps: Evaluation and Application for Snowpack Modeling, J. Hydrometeor., 17, 2591–2614, https://doi.org/10.1175/JHM-D-15-0241.1, 2016.

Vionnet, V., Marsh, C. B., Menounos, B., Gascoin, S., Wayand, N. E., Shea, J., Mukherjee, K., and Pomeroy, J. W.: Multi-scale snowdrift-600 permitting modelling of mountain snowpack, The Cryosphere, 15, 743–769, https://doi.org/10.5194/tc-15-743-2021, 2021.

Voordendag, A., Réveillet, M., MacDonell, S., and Lhermitte, S.: Snow model comparison to simulate snow depth evolution and sublimation at point scale in the semi-arid Andes of Chile, The Cryosphere, 15, 4241–4259, https://doi.org/10.5194/tc-15-4241-2021, 2021a.

Voordendag, A., Goger, B., Klug, C., Prinz, R., Rutzinger, M., Sauter, T., and Kaser, G.: Uncertainty assessment of a permanent long-range terrestrial laser scanning system for the quantification of snow dynamics on Hintereisferner (Austria), Front. Earth Sci., 11, 605 https://doi.org/10.3389/feart.2023.1085416, 2023a.

Voordendag, A., Prinz, R., Schuster, L., and Kaser, G.: Brief communication: The Glacier Loss Day as indicator for extreme glacier melt in 2022, The Cryosphere Discussions, 2023, 1–7, https://doi.org/10.5194/tc-2023-49, 2023b.

Voordendag, A. B., Goger, B., Klug, C., Prinz, R., Rutzinger, M., and Kaser, G.: AUTOMATED AND PERMANENT LONG-RANGE TERRESTRIAL LASER SCANNING IN A HIGH MOUNTAIN ENVIRONMENT: SETUP AND FIRST RESULTS, ISPRS Annals of 610 the Photogrammetry, Remote Sensing and Spatial Information Sciences, V-2-2021, 153–160, https://doi.org/10.5194/isprs-annals-V-2-2021-153-2021, 2021b.

Walter, M. T., McCool, D. K., King, L. G., Molnau, M., and Campbell, G. S.: Simple snowdrift model for distributed hydrological modeling, J. Hydrol. Eng., 9, 280–287, 2004.

Xu, C., Li, Z., Li, H., Wang, F., and Zhou, P.: Long-range terrestrial laser scanning measurements of annual and intra-annual mass balances 615 for Urumqi Glacier No. 1, eastern Tien Shan, China, The Cryosphere, 13, 2361–2383, https://doi.org/10.5194/tc-13-2361-2019, 2019.

Zemp, M., Hoelzle, M., and Haeberli, W.: Six decades of glacier mass-balance observations: a review of the worldwide monitoring network, Ann. Glaciol., 50, 101–111, https://doi.org/10.3189/172756409787769591, 2009.